Published in final edited form as:

Curr Biol. 2020 June 22; 30(12): 2353–2362.e3. doi:10.1016/j.cub.2020.04.015.

The Reissner Fiber is Highly Dynamic *in vivo* and Controls Morphogenesis of the Spine

Benjamin R. Troutwine[1], **Paul Gontarz**[3], **Mia J. Konjikusic**[1], **Ryoko Minowa**[1], **Adrian Monstad-Rios**[4,5], **Diane S. Sepich**[3], **Ronald Y. Kwon**[4,5], **Lilianna Solnica-Krezel**[3], **Ryan S. Gray**[1,2,*]

[1]Department of Pediatrics, Dell Pediatric Research Institute, University of Texas at Austin Dell Medical School, 1400 Barbara Jordan Blvd, Austin, TX 78724 USA.

[2]Department of Nutritional Sciences, University of Texas at Austin, 103 W. 24th Street, TS Painter Hall Austin, TX 78712, USA.

[3]Department of Developmental Biology, Washington University School of Medicine, 660 S. Euclid Avenue Campus Box 8103 St. Louis, MO 63110, USA.

[4]Department of Orthopedics and Sports Medicine, University of Washington, 1959 N.E. Pacific St., Box 356500 Seattle, WA 98195, USA.

[5]Institute for Stem Cell and Regenerative Medicine, University of Washington, Gerberding Hall G80, Box 351202, Seattle, WA 98195, USA.

Summary

Cerebrospinal fluid (CSF) physiology is important for the development and homeostasis of the central nervous system and its disruption has been linked to scoliosis in zebrafish [1, 2]. Suspended in the CSF is an extracellular structure called the Reissner fiber, which extends from the brain through the central canal of the spinal cord. Zebrafish *scospondin* null mutants are unable to assemble a Reissner fiber and fail to form a straight body axis during embryonic development [3]. Here we describe hypomorphic missense mutations of *scospondin*, which allow Reissner fiber assembly and extension of a straight axis. However, during larval development these mutants display progressive Reissner fiber disassembly, which is concomitant with the emergence of axial curvatures and scoliosis in adult animals. Using a *scospondin-GFP* knock-in zebrafish line, we demonstrate several dynamic properties of the Reissner fiber *in vivo*, including embryonic fiber assembly, the continuous rostral to caudal movement of the fiber within the brain and central canal, and SCO-spondin-GFP protein secretion from the floor plate to merge with the fiber. Finally, we show that disassembly of the Reissner fiber is also associated with the progression of axial curvatures in distinct scoliosis mutant zebrafish models. Together these data demonstrate a

*Lead Contact: ryan.gray@austin.utexas.edu.

Author contributions

R.S.G., D.S., and L.S.K. set up the forward genetic screen and isolated the *scospondin* mutant alleles, P.G. and R.S.G. performed WGS/WES and mapping of the mutants, A.M-R. and R.K. performed microCT imaging and analysis, B.T. and M.K. performed immunohistochemistry, confocal imaging, and statistical analysis, B.T. engineered the *scospondin-GFP* knock in , with help with screening and genotyping by R.M., R.S.G. and L.S.K. funded and supervised the project. R.S.G. conceived the project and wrote the article with input from B.T., R.K., D.S., and L.S.K.

Declaration of Interests

The authors declare no competing interests

critical role for the Reissner fiber for the maintenance of a straight body axis and spine morphogenesis in adult zebrafish. Our study establishes a framework for future investigations to address the cellular effectors responsible for Reissner fiber-dependent regulation of axial morphology.

Keywords

Reissner fiber; scoliosis; SCO-spondin; zebrafish

Results and Discussion

Adolescent idiopathic scoliosis (AIS) is a common disorder causing curvature of the spine. Despite accumulating evidence pointing to its heritable nature, the underlying genetic causes of AIS are thought to be complex and heterogenous and thus far are not well established. Zebrafish mutants in motile cilia components with disruption of cerebrospinal fluid (CSF) flow also demonstrate scoliosis, resembling AIS [1, 2]. For example, the expression of AIS-associated variants of the centrosomal protein gene *POC5* led to cilia defects in cell culture and spine deformities in zebrafish [4, 5]. How motile cilia and CSF flow contribute to the pathogenesis of scoliosis in these models remains unresolved.

The Reissner fiber (RF) is an enigmatic glycoprotein thread suspended in CSF, which stretches from the brain down the central canal where it terminates at the base of the spinal cord [6, 7]. The fiber is largely composed of the glycoprotein SCO-spondin [8], which is expressed and secreted from the sub-commissural organ (SCO) of the brain and the floor plate at the ventral midline of the spinal cord [9, 10]. In zebrafish, *scospondin* null mutants fail to secrete and assemble a RF and fail to develop a straight body axis during embryonic development [3]. The failure to straighten the body axis or ‘curled tail down’ phenotype has long been observed in zebrafish mutants with disrupted motile cilia physiology [11–13], many of which also exhibit defects in RF assembly [3]. Despite the clear association of the RF with morphogenesis of a straight body axis, it is not yet clear how disruptions of these processes regulate spine morphogenesis during larval development and in adults.

Hypomorphic mutations of *scospondin* lead to progressive scoliosis in zebrafish

In a forward genetic screen for adult-viable scoliosis mutant zebrafish (unpublished), we found two non-complementing scoliosis mutant zebrafish lines (Figure 1B, B’ and S1B–E). Using whole genome or whole-exome based sequencing, mapping, and variant calling (Figure S1H, I), we identified two recessive missense alleles of the *scospondin* gene, $scospondin^{stl297}$ and $scospondin^{stl300}$, which both disrupt evolutionarily conserved cysteine residues at independent regions of the protein (Figure S1J–L). In cross of either $scospondin^{stl297/+}$ or $scospondin^{stl300/+}$ heterozygotes produced morphologically normal embryos at 1 dpf; however, at 3 dpf we observed the onset of progressive axial curvatures (Figure 1F), which lead to spine curvatures observed in the dorsal-ventral (Figure 1B and S1B) and medial-lateral (Figure 1B’ and S1B’) axes in adult fish. This scoliosis phenotype

was observed without obvious vertebral malformation or alterations in the development of cartilage or bone in the axial skeleton (Figure S1C, D), resembling aspects of AIS in humans. Complementation testing between *scospondin*$^{stl297/+}$ and *scospondin*$^{stl300/+}$ heterozygotes resulted in putative transheterozygous *scospondin*$^{stl297/stl300}$ progeny manifesting curvatures of the body axis resembling those observed for each homozygous mutant outlined above (22.7%, n=198, Figure S1E).

scospondin$^{icm13/icm13}$ null mutants display severe defects in axial straightening at 3 dpf and were not reported to be adult viable [3]. To further determine the nature of the *scospondin*^{stl297} and *scospondin*^{stl300} alleles, we crossed *scospondin*$^{stl297/+}$ heterozygous mutants to heterozygous *scospondin*$^{hsc105/+}$ null mutants, which phenocopy the axis straightening defect reported for *scospondin*$^{icm13/icm13}$ mutant (*scospondin*^{hsc105} described in Rose et al., co-submission). For the progeny resulting from these crosses, we observed no defects in straightening the body axis in embryos. Instead putative transheterozygous *scospondin*$^{hsc105/stl297}$ mutant larvae displayed only mild axial curvatures at 15 dpf (27.1%, n=236); which was identical to phenotypes observed in both zygotic and maternal zygotic *scospondin*$^{stl297/stl297}$ *and scospondin*$^{stl300/stl300}$ mutants (Figure 1D and S1E). Altogether these results confirm that *scospondin*^{stl297} and *scospondin*^{stl300} are independent hypomorphic missense mutations of *scospondin*.

MicroCT analysis in developmentally-matched adult zebrafish at 90 dpf revealed that *scospondin*$^{stl297/stl297}$ and *scospondin*$^{stl300/stl300}$ mutants exhibited abnormalities in bone morphology and mineralization (Figure S2). On average, patterns of sagittal and lateral displacements from midline were similar in both mutants, yet more severe in posterior vertebrae (Figure S2B–C, B'–C'). Analysis of several measures of bone quality in both *scospondin*$^{stl297/stl297}$ and *scospondin*$^{stl300/stl300}$ mutants demonstrated increased bone deposition in the vertebrae in these mutants compared to heterozygous control animals for each allele. For more in-depth morphometric analysis of the spine, we used the FishCut analysis workflow on our microCT datasets [14]. First, segmenting 16 distinct vertebral bodies along the spine and each vertebra into the three elements: the centrum, the haemal arch, and the neural arch (Figure S2N'). Second, we quantified (i) vertebral mass, as total volume and thickness (Figure S2E–G, K–M and E'–G', K'–M'); and (ii) bone quality, as tissue mineral density in comparison to a hydroxyapatite (HA) standard (mgHA/cm3) (Figure S2H–J and H'–J'). These data demonstrated an overall increase in vertebral mass and mineralization in both *scospondin*$^{stl297/stl297}$ and *scospondin*$^{stl300/stl300}$ mutant fish (Figure S2). We observed no change in centrum length comparing homozygous *scospondin* mutants and heterozygous controls (Figure S1D, D'), indicating that decreased body lengths observed in the mutant fish are attributable to spine curvature, rather than shortened or compressed vertebrae. Analysis of z-scores for each of these morphometric measures of the vertebral bodies and spine demonstrated that *scospondin*$^{stl297/stl297}$ mutants display a more severe scoliosis (measured as sagittal and lateral displacement of the spine), while *scospondin*^{stl300} mutants exhibited increased bone volume and mineralization of the spine (Figure S2O, P). We suggest that this increase in bone deposition is a response to increased mechanical loading of the spine as the deformity progresses.

Prior to the onset of spine morphogenesis, we observed mild axial curvatures of the body and notochord in both *scospondin*$^{stl297/stl297}$ and *scospondin*$^{stl300/stl300}$ and transheterozygous *scospondin*$^{stl297/stl300}$ mutants (Figure 1D, S1E). To quantify the onset of body axis curvatures throughout development, we assayed a full complement of combinatorial crosses using both homozygous and heterozygous *scospondin*^{stl297} mutant animals to test whether maternal contributions of SCO-spondin would alter the onset of axial curvatures. For all crosses, regardless of maternal *scospondin* genotype, we observed the onset of progressive axial curvatures, which were first apparent at 3 dpf and fully penetrant at expected mendelian ratios by 20 dpf (Figure 1F). Next, we asked whether the location of axial curvatures along the rostral-caudal axis was stereotyped in *scospondin*^{stl297} mutants. The absolute value of notochord displacement at each somite boundary was propagated along the entire axis in both *scospondin*$^{stl297/stl297}$ mutants and heterozygous controls (Figure 1 E). We measured the dorsal-ventral displacement (y-axis) against an origin established at the intersection of the first somite boundary and the dorsal edge of the notochord for each animal (Figure 1E'). In control larvae, we observed stereotyped axial morphology that corresponded with tight average values of displacement at each somite boundary (n=10), which when graphed illustrated a stereotyped notochord shape consistently observed in wild-type larvae at 5 dpf (Figure 1C, E). In contrast, *scospondin*^{stl297} mutants showed wider ranges of phenotypes from straight body axis to more pronounced axial curvatures (Figure 1D), which was reflected as increased average displacement values along the rostral to caudal axis (n=23). Together these data demonstrate that the formation of axial curvatures is a progressive phenomenon in *scospondin*^{stl297} mutants and that the incidence of axial curvatures along the rostral-caudal axis is a stochastic process, not regionally localized.

Disassembly of the Reissner fiber due to defects in secretion from the floor plate are correlated with the onset of axial curvatures in zebrafish

Scospondin protein is a large, heavily glycosylated protein composed of several repeating, well-conserved domains, established early in phylogeny (Figure 1G, S1L) [10, 15]. *scospondin*^{stl297} mutant phenotype segregates with a T6784A (ENSDART00000097773.4) mutation (Figure S1J), predicted to alter an evolutionarily conserved cysteine 2262 to serine (C2262S) in one of the low-density lipoprotein (LDL) receptor domains of the SCO-spondin protein (Figure 1H, S1L). *scospondin*^{stl300} phenotype segregates with a T2635A mutation (Figure S1K), predicted to alter cysteine 879 to serine (C879S), which is a highly-conserved cysteine adjacent to a trypsin inhibitor like cysteine-rich domain (Figure 1J, S1L). Homology modeling of the *Danio rerio* SCO-spondin protein sequence partially maps onto a crystal structure of very low-density lipoprotein receptor (6byv). Analysis of the model suggests that the *scospondin*^{stl297} mutation could disrupt an evolutionarily conserved disulfide bond (CysIV-CysVI) of the LDL receptor type A motif (Figure 1H, I), shown to be involved in protein stability of the LDL receptor [16]. Homology modeling for the region containing the *scospondin*^{stl300} mutation was unsuccessful, however this cysteine is also neighboring many other well-conserved cysteine residues in SCO-spondin suggesting it may also have a role in disulfide bonding.

To observe the RF assembly in *scospondin* mutant zebrafish, we utilized an established antiserum raised against bovine RF (AFRU) [17], which labels the RF, the floor plate, and terminal ampulla region at the base of the spinal cord in zebrafish (Figure 2A, C). In contrast to *scospondin*$^{icm13/icm13}$ mutants, which fail to form a fiber at 3 dpf [3], *scospondin*$^{stl297/stl297}$ mutant embryos displayed no obvious defects in the assembly of the RF (Figure 2B)(n=8). However, at 5 dpf several *scospondin*$^{stl297/stl297}$ mutants displayed a variety of defects of the RF (Figure 2F) including: irregular punctate pattern (Figure 2E'); disassembled fiber with an occasional bolus of Reissner material (Figure 2E"); or disassembled fiber with diffuse AFRU staining (Figure 2D–D', E'"). We also observed several *scospondin*$^{stl297/stl297}$ mutants displaying a normal fiber at 5 dpf (Figure 2E). *scospondin*$^{stl297/+}$ larvae showed no changes in RF expression at 5 dpf (n=16) (Figure 2C–C'). Interestingly, the presence of an intact RF in *scospondin*$^{stl297/stl297}$ mutants was directly correlated with a straight body axis at 5 dpf, in contrast defects in the RF were directly correlated with the mild to severe axial curvatures in these mutants. At 10 dpf, *scospondin*$^{stl297/+}$ heterozygous mutant larvae (100%, n=8) displayed a straight body axis with an intact RF (Figure 2G–H). In contrast, *scospondin*$^{stl297/stl297}$ mutants displayed diffuse AFRU-staining, without a RF (100%, n=8) (Figure 2I–J). Interestingly, we observed apical-localization of AFRU-stained Reissner material in floor plate cells in heterozygous *scospondin*$^{stl297/+}$ (n=8) and *scospondin*$^{stl300/+}$ (n=7) larvae at 10 dpf (Figure 2G', H and S1F). In contrast, we consistently observed the Reissner material localization at the basal surface of floor plate cells in both *scospondin*$^{stl297/stl297}$ (n=8) and *scospondin*$^{stl300/stl300}$ (n=6) mutants at 10 dpf (Figure 2I and S1G). These data suggest that disassembly of the RF in the two hypomorphic *scospondin* mutants may be in part due to disrupted secretion of Reissner material from the floor plate.

Zebrafish mutants that fail to form a floor plate display defects of RF assembly within the central canal but not within the SCO [18]. We have shown that mutation of two independent, evolutionarily-conserved cysteine residues in SCO-spondin led to disassembly of the RF, axial curvatures in larval fish, and AIS-like scoliosis in adults. We hypothesize that the apical to basal switch in Reissner material polarity in the floor plate cells is the result of disrupted disulfide bonding within the protein leading to unfolded mutant SCO-spondin, which impedes SCO-spondin/Reissner material secretion from the SCO and floor plate, preventing normal RF assembly. Altogether, these data suggest that the RF has a continuous and instructive role in axial straightness and spine morphogenesis in zebrafish.

Dynamic properties of the Reissner fiber revealed in *scospondin-GFP*^{ut24} knock-in zebrafish

To monitor the dynamic properties of the RF during development we engineered an endogenous C-terminal GFP gene fusion of *scospondin* in zebrafish. In brief, we used CRISPR/Cas9 to generate a targeted double strand break within the last exon of the *scospondin* gene and an EGFP donor cassette with homology arms for in-frame C-terminal tagging (Figure S3A). From the resulting adult F0 fish, we isolated a single founder male by (i) PCR screening for EGFP sequence in genomic DNA from isolated sperm samples; (ii) by confocal imaging of outcrossed progeny; and (iii) by colocalization with AFRU

immunofluorescence (Figure S3F–H)(see methods). Imaging of our established stable line (*scospondin-GFP*^{ut24}), showed SCO-spondin-GFP expression *in vivo* labeling of the laser straight RF extending from the SCO in the brain, extending down the central canal and terminating at the base of the spinal cord at 3dpf (Figure S3B, B'). This endogenous SCO-spondin-GFP expression mirrors previously reported tissue specific expression patterns in zebrafish using RF antibodies and whole-mount *scospondin* gene expression [3, 10]. In our hands, SCO-spondin-GFP expression observed in *scospondin-GFP*^{ut24}, knock-in zebrafish displayed tight colocalization (Pearson's R value, 0.98) with the AFRU antiserum labeling [17] (Figure S3F–H). High magnification confocal time-lapse imaging of the floor plate in *scospondin-GFP*^{ut24} embryos demonstrated active secretion of SCO-spondin-GFP from the floor plate to merge with the RF (Figure S3I, Video S1), which supports a critical role for the floor plate in RF assembly during larval development. These observations also suggest that defects in apical localization of the AFRU-labeled Reissner material in *scospondin*^{stl297} mutants (Figure 2I') may be driving progressive disassembly of the RF. In the head, we observed SCO-spondin-GFP expression in the SCO and in the flexural organ, with the RF joining these two organs (Figure 3A, A' and S3C– C'). In the tail, we detected SCO-spondin-GFP expression in the floor plate, and the RF ending as a coiled mass within the terminal ampulla at the base of the spinal cord (Figure 3C, C' and S3B'). We observed SCO-spondin-GFP labeled RF and terminal ampulla in young adult fish (60 dpf) (Figure S3D, D'), suggesting that the RF functions through the life cycle in zebrafish.

To define the natural history of the RF assembly during embryonic development we used confocal time lapse imaging of *scospondin-GFP*$^{ut24/+}$ embryos from the early tailbud stage (~17 hours post fertilization (hpf)). We first observed the assembly of short SCO-spondin-GFP fibers at the rostral portions of the spinal canal between 20–24 hpf (red bracket, Figure 3F and Video S2), which could rapidly extend more caudally (red bracket, Figure 3G, H). SCO-spondin-GFP puncta were also observed to travel in a rostral to caudal direction (red arrows, Figure 3I, J), and appeared to join with other SCO-spondin-GFP material at the end of the spinal cord (Figure 3K). Using higher magnification, we also discerned that fiber formation is preceded by bolus of Reissner material traveling from the head to tail down the central canal, and observed that SCO-spondin-GFP puncta leading the extension of the RF down the central canal (Figure 3L; Video S2). These movements appeared somewhat sporadic as the RF material could stall in place for up to 20 minutes before continuing down the central canal. Motile cilia dependent bi-directional CSF flow in zebrafish is first observed within the central canal at 24-26 hpf [19]. We speculate that the combination of bulk CSF secretion and its flow within the central canal is helping the push the bolus of RF material and the RF along the central canal. After the fiber is formed, during active axis elongation (between 2-3 dpf), we observed the dynamic breakdown of the RF in the terminal ampulla and distribution of SCO-spondin-GFP signal outward into the developing fin fold (Video S3).

It has long been suspected that the RF continually grows in a rostral-caudal direction throughout the life cycle [20], which is supported by the observations of rostral-caudal transport of radiolabeled-monoamines along the fiber in rat [21], and our observations of RF movement during embryonic development in *scospondin-GFP*$^{ut24/+}$ embryos (Figure 3F–L). To directly quantify RF motility during zebrafish development, we photobleached the RF in

the head and tail regions in *scospondin-GFP$^{ut24/+}$* embryos (Figure 3B, D and Video S4). At all stages of development that we assayed, the photobleached regions of the RF consistently traveled in a continuous rostral to caudal direction in the brain (Figure 3B) and tail regions (Figure 3D). In the brain, we observed that the average speed of RF motility at 3 and 5 dpf was 58.6±14.3 and 40.3+5.6 nm/sec respectively (Figure 3B, E). Within the tail region we found the average speed of RF motility at 3 dpf was 220±87 nm/sec, while at 5 and 7 dpf the speed was markedly slower (70±14 nm/sec and 70±24 nm/sec, respectively; t-test; $p=1.3\times10^{-5}$; Figure 3D, E). Using high-speed imaging (10Hz) at higher magnification we also detected rapid movement of SCO-spondin-GFP-labeled puncta moving sporadically down the RF in a rostro-caudal direction, some of which occasionally extended away from the fiber towards the floor plate and retracted back into the bulk RF (Figure S3E, Video S5).

Our *in vivo* analyses of endogenous SCO-spondin-GFP expression and dynamics demonstrates several new properties of the RF including: (i) the initial secretion of Reissner material travels as punctate material from the brain, which precedes the elaboration of the fiber; (ii) we directly confirm the hypothesis that the RF continually moves in a rostral-caudal direction at multiple stages of development; (iii) we evidenced active break down of the RF at terminal ampulla; and (iv) the RF is a conduit for the rapid migration of substances in the CSF in a rostral-caudal direction; and (v) SCO-spondin secretion from the floor plate contributes to RF assembly. The *scospondin-GFP^{ut24}* knock-in zebrafish line, which allows for analysis of dynamic properties of the RF *in vivo* sets the stage for future studies aimed at defining molecular interactions of the Reissner fiber and the dynamics of central canal components with which the RF interacts to regulate axial morphogenesis.

Loss of the Reissner fiber is associated with scoliosis in additional independent scoliosis mutant zebrafish strains

As *scospondin-GFP^{ut24}* is an endogenous gene fusion of the wild-type *scospondin* locus, we are currently precluded from dynamic imaging of the RF in the hypomorphic *scospondin* mutants reported here. However, there are obvious phenotypic similarities between *scospondin* hypomorphic mutants and other cilia-related scoliosis mutants described previously [1, 2]. For this reason, we hypothesized that the loss of the RF may be a common phenotype associated with the onset of scoliosis in independent scoliosis mutant zebrafish in our collection. To test this, we first crossed *scospondin-GFP^{ut24}* to a dominant enhancer-trap transgenic scoliosis mutant, *Et(druk-GFP$^{dut26/+}$)*(Gray, R.S., McAdow, A.R., Solnica-Krezel, L. and Johnson, S.L., unpublished). This mutant was generated by a fortuitous, Tol2-GFP integration on *Danio rerio* Chromosome 11 landing between the *MON1 secretory trafficking family member A* and *macrophage stimulating 1 receptor b* genes. *Et(druk-GFP$^{dut26/+}$)* fish also display a unique GFP-expression pattern in the brain and spinal cord (not shown and Figure 4C'), which is tightly linked with the onset of axial curvatures around 15-18 dpf (Figure 4C) and adult-viable scoliosis (98%; *n=981*). At 5 dpf, the majority of *Et(druk-GFP$^{dut26/+}$);scospondin-GFP$^{ut24/+}$* larvae showed a fully assembled RF (n=6/6)(Figure 4A–A'). At the onset of axial curvatures in these mutants, we observed a consistent loss of the SCO-spondin-GFP labeled RF (100% of fish at 6.1-7.0 mm; n=9)(Figure 4D, D'). In contrast similarly sized *scospondin-GFP$^{ut24/+}$* knock-in larvae always displayed a typical RF

(100% of fish sized 6.3-6.8 mm; n=9)(Figure 4B, B'). While the molecular genetics of the dominant *Et(druk-GFP$^{dut26/+}$)* scoliosis mutant remains to be defined, we do provide direct evidence that the disassembly of the SCO-spondin-GFP labeled RF in real-time, in a living animal, is coincident with the onset of axial curvatures and scoliosis in these mutants.

Mutations in the zebrafish *kinesin family member 6* (*kif6*) gene cause scoliosis without vertebral malformations in adult zebrafish. We first assayed the RF using AFRU immunostaining in *kif6$^{sko/sko}$* mutants at 1 dpf and found no defects in the assembly of the RF, in comparison to heterozygous *kif6$^{sko/+}$* control embryos (Figure 4E, F). By 3 dpf *kif6$^{sko/sko}$* mutant embryos display mild axial curvatures [22], concurrently we observed the complete disassembly of the RF (Figure 4H) within the central canal (Figure 4H'). In contrast to the absent or diffuse staining observed in *scospondin^{stl297}* mutants (Figure 2E'", F), we consistently detected the AFRU-stained Reissner material filling up the entire central canal in *kif6^{sko}* mutants at both 3 and 5 dpf (Figure 4H" and J), suggesting that the secretion of the material is not affected, rather its ability to polymerize in the central canal is disrupted. Defects in motile cilia components give rise to defects in RF formation in zebrafish embryos [3] and the motile ciliated ependymal cell cilia are lost in adult *kif6* mutants [1]. This suggests that alterations in CSF flow may underlying the loss of RF polymerization in *kif6^{sko}* mutants. However, bulk CSF flow is grossly unaffected in *kif6* mutant embryos [22], suggesting alternative models of *kif6* regulation for RF assembly are possible. Altogether our observations of RF disassembly in three independent scoliosis mutants strongly supports the critical role of the RF structure to regulate the homeostasis of the straight body axis and for spine morphogenesis in zebrafish. Additional studies focused on the elucidation of cellular and molecular differences related to RF disassembly in these three independent scoliosis mutant strains are warranted.

Since the discovery of the RF multiple hypotheses have been proposed for its function, including detoxification and transport of molecules in CSF [21], neurogenesis during early brain development [23, 24], and through its direct interaction with the ciliated CSF-contacting neurons lining the central canal, as a mechanosensory organ controlling the "flexure of the body" [25, 26]. Early work in amphibians demonstrated that the resection of the SCO disrupted RF assembly and led to scoliosis in some animals [27, 28]. Here, we used forward genetics and cell biology approaches in zebrafish to demonstrate that two evolutionally-conserved cysteine residues in the SCO-spondin protein are critical for stability of the RF during larval development. One of these cysteines (C2262) is predicted to form a disulfide bridge in one of several canonical LDL receptor A domains found in SCO-spondin. Interestingly, the LDL protein Apolipoprotein B has been directly visualized in the central canal in zebrafish [29] and is found in the CSF of rat and humans by proteomic analysis [30–32]. Apolipoprotein B is also an important neurogenic factor *in vitro* [33], is important for brain development in mice [34], and forms a complex with SCO-spondin in the CSF which can synergistically modulate neurodifferentiation in organotypic brain culture [35]. For these reasons, it is tempting to speculate that the C2262S mutation may also disrupt important LDL interactions with the Reissner fiber, causing alterations in neuronal differentiation in *scospondin^{stl297}* mutant zebrafish.

Our results using a variety of genetic models of scoliosis in zebrafish, a novel *scospondin-GFP* knock-in strain, and analysis of cell biology and time-lapse imaging approaches to assay the RF *in vivo* now demonstrate that the intact fiber and its dynamic properties are required for maintaining a straight body axis and spine morphogenesis. Our study opens up a new field of exploration of dynamic properties of the Reissner fiber assembly, of molecular interactions of the fiber and CSF components for axial morphogenesis, and whether this physiology is driving scoliosis in humans.

STAR Methods

LEAD CONTACT AND MATERIALS AVAILABILITY

Further information and requests for *scospondin* mutants (*stl297* and *stl300*), *scospondin-GFP*^{ut24} knock-in zebrafish, or pCS108-*scospondinGFP* donor targeting reagents should be directed to and fulfilled by the Lead Contact Lead Contact, Ryan S. Gray (ryan.gray@austin.utexas.edu).

EXPERIMENTAL MODEL AND SUBJECT DETAILS

Zebrafish Maintenance and Care: All experiments were performed according to University of Texas at Austin with approval of the IACUC committee. All experiments were performed on *Danio rerio* embryos or larval – adult fish of the AB background. Animals were raised at 28.5 °C under a 14/ 10 light/ dark cycle until the start of experiments.

METHOD DETAILS

WGS / WES analysis—Phenotypic, mutant zebrafish were pooled and submitted for sequencing. Non-phenotypic wild type and heterozygous siblings were pooled together and submitted for sequencing. Raw reads were aligned to zebrafish genome GRCz10 using bwa mem (v0.7.12-r1034) with default parameters and were sorted and compressed into bam format using samtools (v1.6) [36]. Variants were called using bcftools (v1.9) functions mpileup, call, and filter. mpileup parameters “-q 20” and “-Q 20” were set to require alignments and base calls with 99% confidence to be used and filter parameters “-s LowQual -e ′%QUAL<20’” were used to remove low quality variant calls. Variants were then annotated and filtered by an in-house pipeline. Briefly, variants occurring with the same allele frequency between phenotypic and aphenotypic samples were filtered from further analysis as were variants that were not called as being homozygous in the phenotypic sample. Variants in the mutant samples that were homozygous for the wild type allele were also excluded. Variants found in the dbSNP database (build v142) of known variants were also filtered out and excluded from further analysis. The wild type and mutant alleles at each variants site were tabulated, and the Fisher p-value was calculated for each variant site. These remaining variants classified based on their genomic location as being noncoding site variants, coding site variants, or variants that may affect gene splicing using zebrafish Ensembl annotation build v83. For coding site variants, the amino acid of the wild type allele and the mutant allele were determined from the Ensembl annotation. The p-values were plotted against genomic location, and a region of homozygosity in the genome with a cluster of small p-values was found. Variants occurring within this region of homozygosity were manually prioritized for nonsynonymous mutations in genes.

MicroCT scanning and analysis—MicroCT scanning was performed as previously described [14]. All analyses were performed in precaudal and caudal vertebrae only (we refer to the 1st precaudal vertebrae as vertebra 1). For analysis of spinal curvature, centrum centroid positions were identified in maximum intensity projections. A line was drawn connecting the first and last vertebrae. The absolute value of the displacements from this line were computed in the sagittal and frontal planes to compute Sagital Displacement (Sag.Disp) and Lateral Displacement (Lat.Disp) for vertebrae 1-20. For analysis of bone, FishCuT was used to quantify Length (Le), Volume (Cent.Vol), Tissue Mineral Density (TMD), and Thickness (Th) in the Centrum (Cent), Neural Arch (NA), and Haemal Arch (Haem) for vertebrae 1-16 [14]. Computation of standard scores, z-scores, and statistical testing using the global test were performed as previously described [14, 37].

Generation of endogenously tagged scospondin-GFP^{ut24} allele—CRISPR/Cas9 targets were chosen using CHOPCHOP and guides were synthesized according to the CHOPCHOP protocols [38]. The last exon of *scospondin* was targeted with the CRISPR guide AGTGTACCAGCTGCCAGGGTGGG (PAM underlined) predicted to cut 6 bp upstream of the stop codon. To generate an sgRNA guide, an oligo (Scospondin_stop_sgRNA) containing a T7 promoter, gene-specific targeting sequence, and annealing region was synthesized (Sigma-Aldrich). This oligo was annealed to a generic CRISPR oligo using CloneAmp Hifi Polymerase. RNA was synthesized using the NEB HiScribe T7 RNA synthesis kit and purified with the Zymo RNA Clean and Concentrator-5 kit.

A plasmid was constructed to serve as a donor. The plasmid contained 5’ and 3’ homology arms (776 and 532 bp respectively) flanking the eGFP coding sequence (720bp). The donor was constructed such that the PAM would be abolished and the eGFP coding sequence would be inserted just before the endogenous stop codon. The homology arms were cloned from wild-type AB zebrafish DNA and eGFP was cloned from the p3E-2AnlsGFP plasmid [39] using Clontech Hifi polymerase mix. These three fragments were purified (NucleoSpin Gel and PCR Clean-up, Machery-Nagel #740609) and Gibson cloned into the EcoRI site of pCS108 using the In-Fusion HD Cloning kit (Clontech) following manufacturer protocols.

Wild type AB zebrafish were incrossed and one-cell embryos were injected with 1nL of injection mix containing 5¼M EnGen Spy Cas9 NLS (NEB #M0646), 100 ng/¼L sgRNA, and 25 ng/¼L donor plasmid. Once the embryos reached adulthood, sperm was collected from F0 males and DNA was extracted by diluting sperm into 50uL of 50mM NaOH and heated to 95°C for 40 minutes, then neutralized with 10uL 1M TRIS. PCR was performed with GFP-specific primers using GoTaq Green Master Mix (Promega #M7123). Males that generate an amplicon after PCR were outcrossed to WT AB females, and the progeny were screened for GFP expression in the SCO and Reissner Fiber.

Skeletal preparation—Animals were euthanized in tricaine and fixed in 10% formalin overnight, then incubated in acetone overnight. Acetone was washed away with water, and animals were stained with Bone/Cartilage Stain (0.015% Alcian Blue, 0.005% Alizarin Red, 5% Acetic Acid, 59.5% Ethanol) at 37°C overnight, and cleared in 1% KOH for days to

weeks depending on the size of the fish. The fish were then moved to 25%, 50%, and then 80% glycerol and imaged.

Immunohistochemistry and live imaging—Animals were euthanized with high dose tricaine (MS-222), and then fixed in sweet paraformaldehyde solution (4% PFA, 4% sucrose in PBS) for 2 hrs at 4°C. Animals were washed in PBSTr (1x PBS with 0.1% Triton X-100), blocked with 10% normal goat serum in 1x PBS with 0.5% Triton X-100 and 1% DMSO. The following primary antibodies were used as follows: Rabbit AFRU primary antibody shared by Esteban Rodriguez (Rodríguez *et al.*, 1984) and at 1:2000 dilution, Mouse anti ZO-1 (Thermo-Fisher #33-9100, RRID: AB_2533147) at 1:250 dilution, and Chicken anti GFP (Abcam ab13970, RRID: AB_300798) at 1:500 dilution in blocking solution overnight at room temperature. Specimens were then washed and stained with the following secondary antibodies at 1:1000 in block: goat anti-rabbit IgG (H+L) Alexa Fluor 488 (Thermo Fisher Cat# A11034, RRID:AB_2576217), goat anti-rabbit IgG (H+L) Alexa 555 (Thermo Fisher Cat# A21428, RRID:AB_2535849), goat anti-chicken IgY (H+L) Alexa 488 (Thermo Fisher Cat# A11039, RRID:AB_2534096), goat anti-mouse IgG1 Alexa 647 (Thermo Fisher Cat# A21240, RRID:AB_2535809); then washed in PBSTr and counterstained with DAPI. Fixed specimens were immobilized in 1% low-melt agarose in 1x PBS. Live embryos or larvae were anaesthetized in 0.16% tricaine for 10 minutes and then embedded in 0.5% low-melt agarose, 0.16% tricaine in egg water for imaging using a humidified incubating stage set to 28.5°C. All confocal images were taken using a Nikon Ti2E / CSU-W1 spinning disc confocal system, with the exception of photobleaching experiments which were performed using a Nikon A1R laser scanning confocal microscope. Post-acquisition analysis was done using standard modification of levels of the entire image file (Nikon .nd2 file) and exported as jpeg's in Fiji (ImageJ).

QUANTIFICATION AND STATISTICAL ANALYSIS

Statistical analysis was performed using GraphPad Prism, and statistical details are given in figure legends.

DATA AND CODE AVAILABILITY

The published article includes all datasets generated or analyzed during this study.

Supplementary Material

Refer to Web version on PubMed Central for supplementary material.

Acknowledgements

We thank Esteban Rodriguez and Maria Montserrat Guerra (Universidad Austral de Chile) for their generous gift of the AFRU antiserum. We thank Chole Rose and Brian Ciruna for generously sharing the *scospondin*^{hsc105} mutant zebrafish prior to publication. We thank Sierra Szkrybalo and Melisa N. Bayrak for assistance with zebrafish experiments. We thank Drs. John Wallingford and Claire Wyart for critical comments this manuscript. We thank the Genome Technology Access Center in the Department of Genetics at Washington University School of Medicine for help with genomic analysis. The Center is partially supported by NCI Cancer Center Support Grant #P30 CA91842 to the Siteman Cancer Center and by ICTS/CTSA Grant# UL1TR002345 from the National Center for Research Resources (NCRR), a component of the National Institutes of Health (NIH), and NIH Roadmap for Medical Research. This publication is solely the responsibility of the authors and does not necessarily represent the official view of NCRR or NIH. Research reported in this publication was supported in part by a grant from Spinal

Cord Injury/Disease Research Program (SCIDRP) (LSK and Steve Johnson), the Scoliosis Research Society (SRS), the National Institute of Arthritis and Musculoskeletal and Skin Diseases of the National Institutes of Health under Award Number AR072009 to (R.S.G.) and AR066061 to (R.Y.K.) and by the National Institute for Child Health and Human Development of the National Institutes of Health under Award Number P01HD084387 (LSK).

References

1. Konjikusic MJ, Yeetong P, Boswell CW, Lee C, Roberson EC, Ittiwut R, Suphapeetiporn K, Ciruna B, Gurnett CA, Wallingford JB, et al. (2018). Mutations in Kinesin family member 6 reveal specific role in ependymal cell ciliogenesis and human neurological development. PLoS Genet 14, e1007817. [PubMed: 30475797]
2. Grimes DT, Boswell CW, Morante NF, Henkelman RM, Burdine RD, and Ciruna B (2016). Zebrafish models of idiopathic scoliosis link cerebrospinal fluid flow defects to spine curvature. Science 352, 1341–1344. [PubMed: 27284198]
3. Cantaut-Belarif Y, Sternberg JR, Thouvenin O, Wyart C, and Bardet PL (2018). The Reissner Fiber in the Cerebrospinal Fluid Controls Morphogenesis of the Body Axis. Curr Biol 28, 2479–2486 e2474. [PubMed: 30057305]
4. Patten SA, Margaritte-Jeannin P, Bernard JC, Alix E, Labalme A, Besson A, Girard SL, Fendri K, Fraisse N, Biot B, et al. (2015). Functional variants of POC5 identified in patients with idiopathic scoliosis. J Clin Invest 125, 1124–1128. [PubMed: 25642776]
5. Hassan A, Parent S, Mathieu H, Zaouter C, Molidperee S, Bagu ET, Barchi S, Villemure I, Patten SA, and Moldovan F (2019). Adolescent idiopathic scoliosis associated POC5 mutation impairs cell cycle, cilia length and centrosome protein interactions. PLoS One 14, e0213269. [PubMed: 30845169]
6. Reissner E (1860). Beiträge zur Kenntnis vom Bau des Rückenmarkes von Petromyzon fluviatilis L. Arch Anat Physiol Wiss Med, Leipzig, 545–588.
7. Munoz RI, Kahne T, Herrera H, Rodriguez S, Guerra MM, Vio K, Hennig R, Rapp E, and Rodriguez E (2019). The subcommissural organ and the Reissner fiber: old friends revisited. Cell Tissue Res 375, 507–529. [PubMed: 30259139]
8. Kohno K (1969). Electron microscopic studies on Reissner's fiber and the ependymal cells in the spinal cord of the rat. Z Zellforsch Mikrosk Anat 94, 565–573. [PubMed: 5809189]
9. Guinazu MF, Richter HG, and Rodriguez EM (2002). Bovine floor plate explants secrete SCO-spondin. Cell Tissue Res 308, 177–191. [PubMed: 12037576]
10. Meiniel O, Meiniel R, Lalloue F, Didier R, Jauberteau MO, Meiniel A, and Petit D (2008). The lengthening of a giant protein: when, how, and why? J Mol Evol 66, 1–10. [PubMed: 18046595]
11. Brand M, Heisenberg CP, Warga RM, Pelegri F, Karlstrom RO, Beuchle D, Picker A, Jiang YJ, Furutani-Seiki M, van Eeden FJ, et al. (1996). Mutations affecting development of the midline and general body shape during zebrafish embryogenesis. Development 123, 129–142. [PubMed: 9007235]
12. Jaffe KM, Grimes DT, Schottenfeld-Roames J, Werner ME, Ku TS, Kim SK, Pelliccia JL, Morante NF, Mitchell BJ, and Burdine RD (2016). c21orf59/kurly Controls Both Cilia Motility and Polarization. Cell Rep 14, 1841–1849. [PubMed: 26904945]
13. Kramer-Zucker AG, Olale F, Haycraft CJ, Yoder BK, Schier AF, and Drummond IA (2005). Cilia-driven fluid flow in the zebrafish pronephros, brain and Kupffer's vesicle is required for normal organogenesis. Development 132, 1907–1921. [PubMed: 15790966]
14. Hur M, Gistelinck CA, Huber P, Lee J, Thompson MH, Monstad-Rios AT, Watson CJ, McMenamin SK, Willaert A, Parichy DM, et al. (2017). MicroCT-based phenomics in the zebrafish skeleton reveals virtues of deep phenotyping in a distributed organ system. Elife 6.
15. Meiniel O, and Meiniel A (2007). The complex multidomain organization of SCO-spondin protein is highly conserved in mammals. Brain Res Rev 53, 321–327. [PubMed: 17126404]
16. Jeon H, and Blacklow SC (2005). Structure and physiologic function of the low-density lipoprotein receptor. Annu Rev Biochem 74, 535–562. [PubMed: 15952897]
17. Rodriguez EM, Oksche A, Hein S, Rodriguez S, and Yulis R (1984). Comparative immunocytochemical study of the subcommissural organ. Cell Tissue Res 237, 427–441. [PubMed: 6435876]

18. Lehmann C, and Naumann WW (2005). Axon pathfinding and the floor plate factor Reissner's substance in wildtype, cyclops and one-eyed pinhead mutants of Danio rerio. Brain Res Dev Brain Res 154, 1–14. [PubMed: 15617750]
19. Sternberg JR, Prendergast AE, Brosse L, Cantaut-Belarif Y, Thouvenin O, Orts-Del'Immagine A, Castillo L, Djenoune L, Kurisu S, McDearmid JR, et al. (2018). Pkd2l1 is required for mechanoception in cerebrospinal fluid-contacting neurons and maintenance of spine curvature. Nat Commun 9, 3804. [PubMed: 30228263]
20. Kolmer W (1921). Das "Sagittalorgan" der Wirbeltiere. Zeitschrift für Anatomie und Entwicklungsgeschichte 60, 652–717.
21. Caprile T, Hein S, Rodriguez S, Montecinos H, and Rodriguez E (2003). Reissner fiber binds and transports away monoamines present in the cerebrospinal fluid. Brain Res Mol Brain Res 110, 177–192. [PubMed: 12591155]
22. Buchan JG, Gray RS, Gansner JM, Alvarado DM, Burgert L, Gitlin JD, Gurnett CA, and Goldsmith MI (2014). Kinesin family member 6 (kif6) is necessary for spine development in zebrafish. Dev Dyn 243, 1646–1657. [PubMed: 25283277]
23. Vera A, Stanic K, Montecinos H, Torrejon M, Marcellini S, and Caprile T (2013). SCO-spondin from embryonic cerebrospinal fluid is required for neurogenesis during early brain development. Front Cell Neurosci 7, 80. [PubMed: 23761733]
24. El-Bitar F, Bamdad M, Dastugue B, and Meiniel A (2001). Effects of SCO-spondin thrombospondin type 1 repeats (TSR) in comparison to Reissner's fiber material on the differentiation of the B104 neuroblastoma cell line. Cell Tissue Res 304, 361–369. [PubMed: 11456412]
25. Dendy A (1909). The Function of Reissner's Fibre and the Ependymal Groove. Nature 82, 217–217.
26. Nicholls GE (1917). Some Experiments on the Nature and Function of Reissner's Fiber. The Journal of Comparative Neurobiology 27.
27. Hauser R (1969). [Dependence of normal tail regeneration in Xenopus larvae upon a diencephalic factor in the central canal]. Wilhelm Roux Arch Entwickl Mech Org 163, 221–247. [PubMed: 28304488]
28. Rühle H-J (1971). Anomalien im Wachstum der Achsenorgane nach experimenteller Ausschaltung des Komplexes Subcommissuralorgan—Reissnerscher Faden. Untersuchungen am Rippenmolch. Acta Zoologica 52, 23–68.
29. Thierer JH, Ekker SC, and Farber SA (2019). The LipoGlo reporter system for sensitive and specific monitoring of atherogenic lipoproteins. Nat Commun 10, 3426. [PubMed: 31366908]
30. Zappaterra MD, Lisgo SN, Lindsay S, Gygi SP, Walsh CA, and Ballif BA (2007). A comparative proteomic analysis of human and rat embryonic cerebrospinal fluid. J Proteome Res 6, 3537–3548. [PubMed: 17696520]
31. Koch M, Furtado JD, Falk K, Leypoldt F, Mukamal KJ, and Jensen MK (2017). Apolipoproteins and their subspecies in human cerebrospinal fluid and plasma. Alzheimers Dement (Amst) 6, 182–187. [PubMed: 28289700]
32. Koch S, Donarski N, Goetze K, Kreckel M, Stuerenburg HJ, Buhmann C, and Beisiegel U (2001). Characterization of four lipoprotein classes in human cerebrospinal fluid. J Lipid Res 42, 1143–1151. [PubMed: 11441143]
33. Parada C, Escola-Gil JC, and Bueno D (2008). Low-density lipoproteins from embryonic cerebrospinal fluid are required for neural differentiation. J Neurosci Res 86, 2674–2684. [PubMed: 18500757]
34. Farese RV Jr., Ruland SL, Flynn LM, Stokowski RP, and Young SG (1995). Knockout of the mouse apolipoprotein B gene results in embryonic lethality in homozygotes and protection against diet-induced hypercholesterolemia in heterozygotes. Proc Natl Acad Sci U S A 92, 1774–1778. [PubMed: 7878058]
35. Vera A, Recabal A, Saldivia N, Stanic K, Torrejon M, Montecinos H, and Caprile T (2015). Interaction between SCO-spondin and low density lipoproteins from embryonic cerebrospinal fluid modulates their roles in early neurogenesis. Front Neuroanat 9, 72. [PubMed: 26074785]

36. Li H, and Durbin R (2009). Fast and accurate short read alignment with Burrows-Wheeler transform. Bioinformatics 25, 1754–1760. [PubMed: 19451168]

37. Gistelinck C, Kwon RY, Malfait F, Symoens S, Harris MP, Henke K, Hawkins MB, Fisher S, Sips P, Guillemyn B, et al. (2018). Zebrafish type I collagen mutants faithfully recapitulate human type I collagenopathies. Proc Natl Acad Sci U S A 115, E8037–E8046. [PubMed: 30082390]

38. Labun K, Montague TG, Gagnon JA, Thyme SB, and Valen E (2016). CHOPCHOP v2: a web tool for the next generation of CRISPR genome engineering. Nucleic Acids Res 44, W272–276. [PubMed: 27185894]

39. Kwan KM, Fujimoto E, Grabher C, Mangum BD, Hardy ME, Campbell DS, Parant JM, Yost HJ, Kanki JP, and Chien CB (2007). The Tol2kit: a multisite gateway-based construction kit for Tol2 transposon transgenesis constructs. Dev Dyn 236, 3088–3099. [PubMed: 17937395]

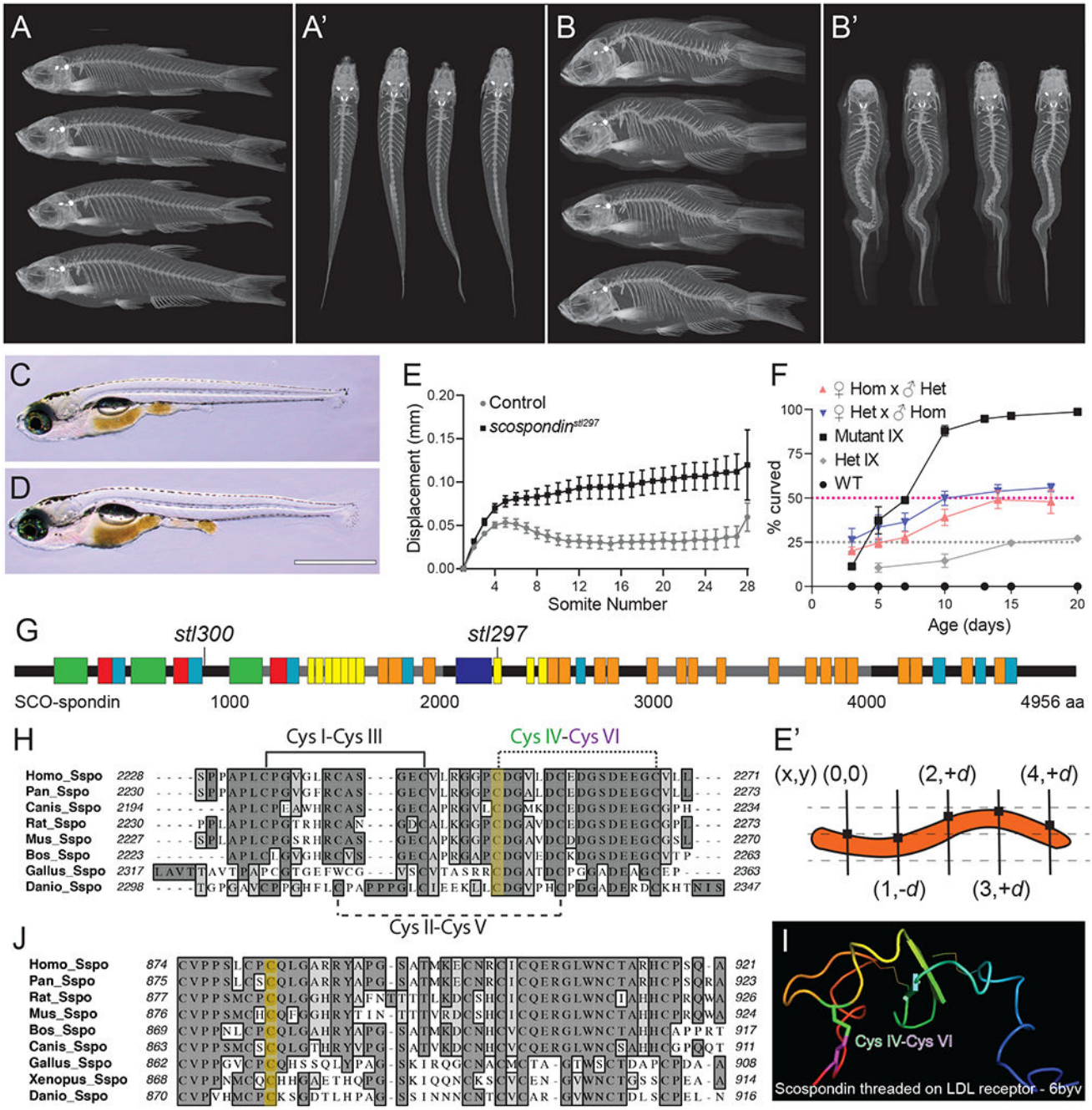

Figure 1. Hypomorphic mutations of *scospondin* lead to progressive scoliosis in zebrafish

(A-B') MicroCT images of *scospondin*$^{stl300/+}$ (A-A') and *scospondin*$^{stl300/stl300}$ mutant zebrafish (B-B') at 90 dpf, in both lateral (A, B) and dorsal (A', B') views showing adult-viable scoliosis.

(C, D) Bright field image of the typical straight body of a wild-type (D) and atypical axial curvatures observed in homozygous *scospondin*$^{stl297/stl297}$ mutant (E) larvae at 13 dpf. Scale bar is 1 mm.

(E) Dorsal-ventral axis displacement of the notochord in 5 dpf heterozygous *scospondin*$^{stl297/+}$ and *scospondin*$^{stl297/stl297}$ mutants (n=10 and 23 respectively). (E') Displacement is the absolute value of the dorsal-ventral (y-axis) measured against an origin set at the intersection of the first somite boundary and the dorsal edge of the notochord and propagated along the entire axis at each somite boundary for each animal.
(F) Incidence of axial curvatures over developmental time for wild type, *MZscospondin*^{stl297}, and progeny from heterozygous *scospondin*$^{stl297/+}$ x *scospondin*$^{stl297/stl297}$ mutant crosses from both female and male homozygotes, and progeny from heterozygous *scospondin*$^{stl297/+}$ incrosses (mean + SD; n=112, 105, 116, 138, and 118 embryos, respectively, pooled from three independent clutches).
(G) Schematic representation of SCO-spondin protein demonstrating the location of the *scospondin* alleles causing with scoliosis in zebrafish. Boxes represent conserved motifs, legend in Figure S1.
(H, J) Protein alignments (Clustal-W) of SCO-spondin protein showing the sequence surrounding the amino acid residues (yellow highlight) affected by the *scospondin*^{stl297} (H) and the *scospondin*^{stl300} (J) mutations.
(I) A homology model of *Danio rerio* SCO-spondin threaded onto the LDLrA domain derived from an LDL receptor structure (6byv). The predicted disulfide bond and labeled cysteine (Cys) residues are highlighted in (H and I).
See also Figure S1–2.

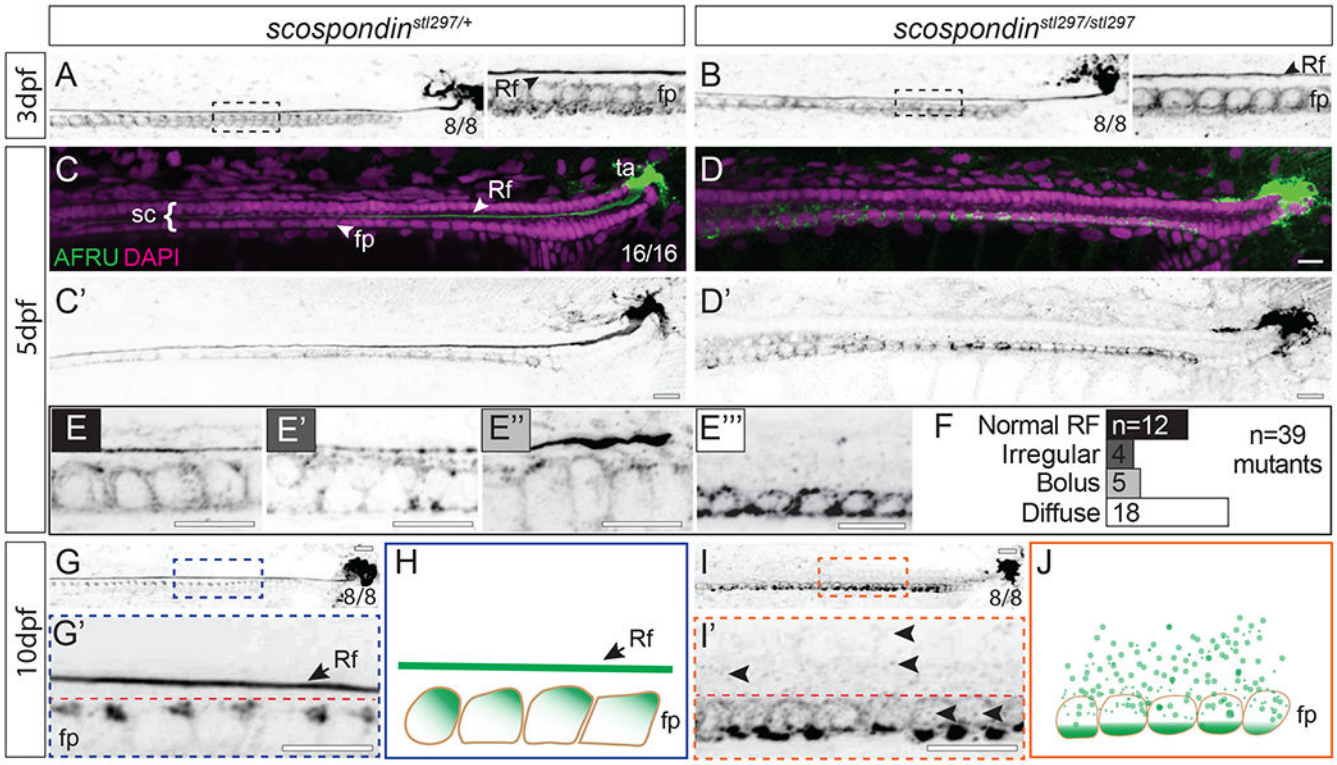

Figure 2. Disassembly of the Reissner fiber due to defects in secretion from the floor plate are correlated with the onset of axial curvatures in zebrafish

Maximal Z-projections of confocal stacks of the caudal region of the tail and spinal cord immunostained against the Reissner fiber in *scospondin*$^{stl297/+}$ and *scospondin*$^{stl297/stl297}$ mutants at 3 dpf (A, B), 5 dpf (C-E'"), and 10 dpf (G, G', I, I'). *Rf* Reissner fiber; *fp* floor plate; *sc* spinal cord; *ta* terminal ampulla.

(A,B) At 3 dpf, both heterozygotes (A) and mutants (B) have an assembled fiber (8/8 each genotype). Insets to the right of panel (A, B) highlight a magnified region (dashed box).

(C-F) Pseudocolored merge from maximal Z-projections of confocal stacks showing Reissner fiber (green) and DAPI (magenta) marking nuclei (C, D) and inverted grayscale image of Reissner fiber at 5 dpf (C', D'). We observed the RF in all heterozygous mutants (100%, n=16) (C) but the *scospondin*$^{stl297/stl297}$ showed some with the fiber (31%, n=39) and some with a fiber in various stages of disassembly (69%, n=39) (D). We classified Reissner fiber staining as Normal (E), irregular (E'), bolus (E"), or diffuse (E'") and counted the number of mutants in each class (F). Scale bars are 10 μm

(G,I) At 10 dpf, we observed the RF in all heterozygous controls (G) which was completely lost in the mutants (I) (100%, n=7, 8, respectively). Scale bars are 10 μm.

(H, J) Schematic representation of Reissner material localization at 10 dpf. In wild-type or heterozygous animals Reissner material localizes to the apical surface of floor plate cells and is assembled into a Reissner fiber (H). In *scospondin*$^{stl297/stl297}$ mutants the Reissner fiber is missing and Reissner material localizes at the basal portion of the floor plate (J).

See also Figure S1–2.

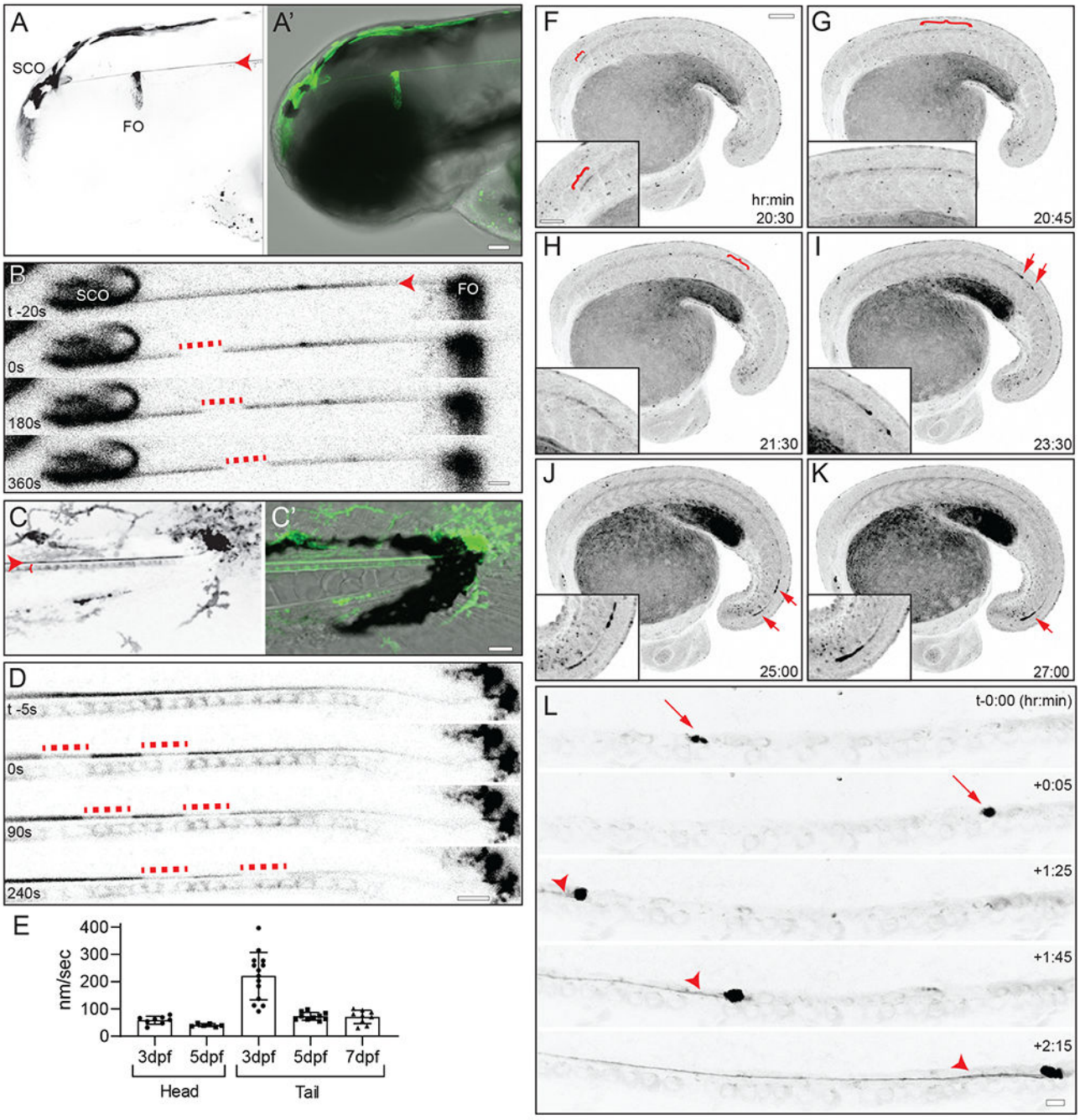

Figure 3. Dynamic properties of the Reissner fiber revealed in *scospondin-GFP^{ut24}* knock-in zebrafish

(A) Inverted greyscale maximal Z-projection of confocal stack of *scospondin-GFP$^{ut24/+}$* embryo at 3 dpf. Expression in the subcommissural organ (SCO) and flexural organ (FO) in the head with Reissner fiber (red arrowhead) (A). Merge of DIC image and pseudocolored SCO-spondin-GFP expression (Green) (A'). Scale bar: 50 μm

(B) Inverted greyscale frames from a time-lapse confocal dataset from a *scospondin-GFP$^{ut24/+}$* embryo head at 3 dpf. At time (t)=0, a region was photobleached using a short,

high energy pulse from a 488nm solid state laser which allowed for manual tracking of the movement of the bleached region from rostral to caudal. Scale bar 10μm.
(C) Inverted greyscale maximal Z-projection of confocal stack of *scospondin-GFP*$^{ut24/+}$ embryo tail at 3 dpf. The Reissner fiber (red arrowhead) and floor plate (red bracket) are labeled with GFP (C). Merge of DIC image and pseudocolored SCO-spondin-GFP expression (Green) (C'). Scale bar 20μm.
(D) Inverted greyscale frames from a time-lapse confocal dataset from a *scospondin-GFP*$^{ut24/+}$ embryo head at 3 dpf. At time (t)=0, two regions were photobleached as in B which allowed for manual tracking of the movement of the bleached region from rostral to caudal. Scale bar 10μm.
(E) Average velocity as nanometers (nm) per second (sec) were calculated manually for multiple embryos at 3, 5, and 7 dpf in experiments depicted in B and D (n=13, 9, and 8 respectively). The average velocity for each individual embryo was plotted as box plots (mean ± SD). (**** denotes p-value $<10^{-4}$)
(F-K) Frames from a time-lapse confocal dataset taken during tail bud development (20-30 hours post fertilization, see Video S2) presented as inverted greyscale maximal Z-projections. Red brackets highlight faint expression, extended fibers of SCO-spondin-GFP, while red arrows point out a bolus SCO-spondin-GFP material which is observed to travel rapidly in a rostral to caudal direction. Inset in the lower left-hand side of each panel are digitally enlarged portions of the region containing SCO-spondin-GFP-labeled material. Scale bars: 100 μm in main, 50 μm in inset. Time stamp is hr:min post-fertilization.
(L) Frames from a time-lapse confocal dataset taken during tail bud development (20-22 hours post fertilization, see Video S2) presented as inverted greyscale maximal Z-projections. Red arrows highlight SCO-spondin-GFP-labeled bolus material, while red arrowheads indicate bolus material leading the Reissner fiber. Scale bars: 10 μm
See also Figure S3 and Video S1–5.

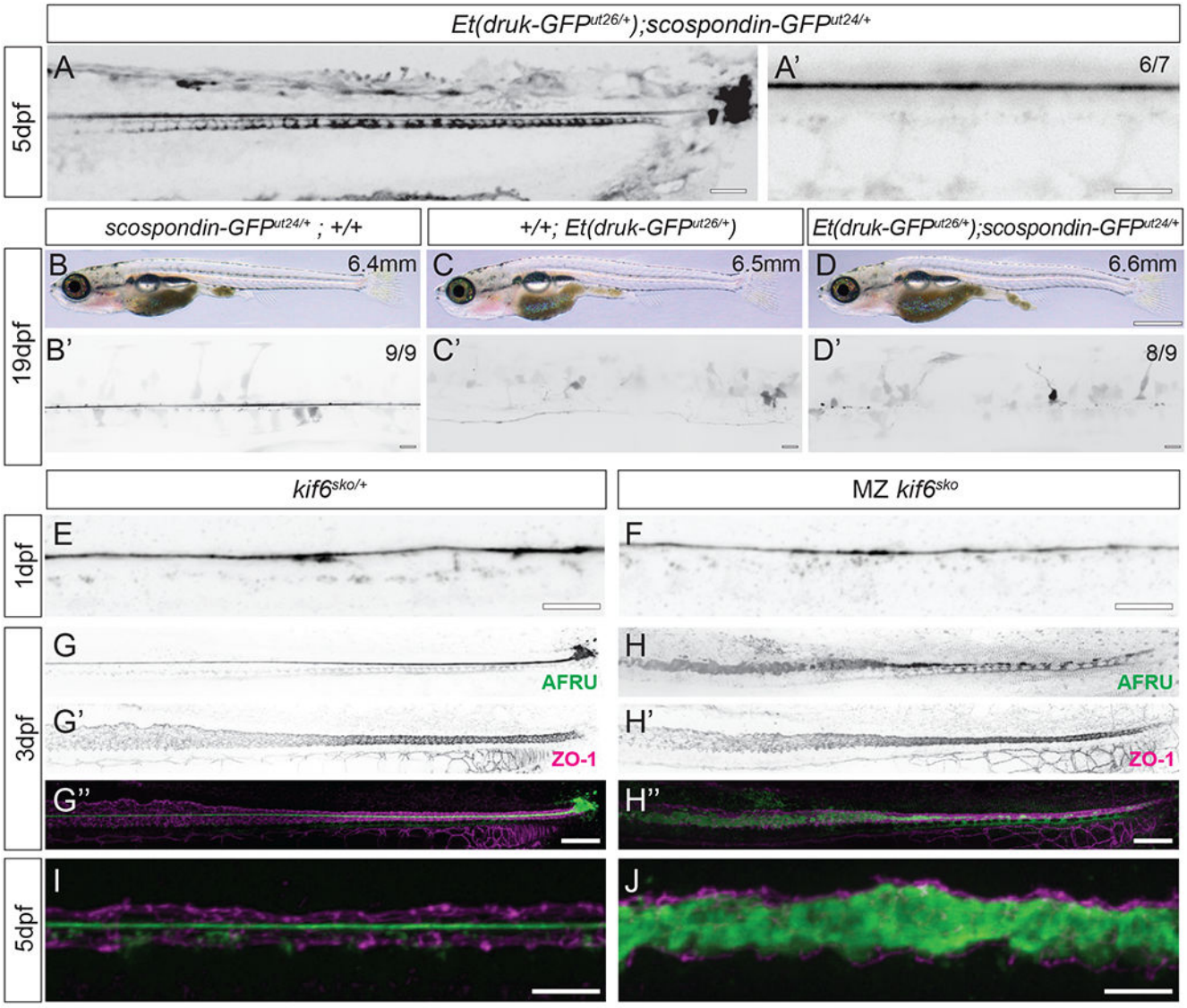

Figure 4. Loss of the Reissner fiber is associated with scoliosis in additional independent scoliosis mutant zebrafish strains.

(A-A') Inverted greyscale maximal Z-projections of confocal images of *Et(druk-GFP$^{dut26/+}$; scospondin-GFP$^{ut24/+}$* demonstrating typical assembly of the Reissner fiber, floor plate and terminal ampulla expression in these mutant knock-in embryos at 5 dpf. *Note that GFP expression is contributed both by the Et(druk-GFP$^{dut26/+}$) transgene insertion and from the scospondin-GFP$^{ut24/+}$ allele.* Scale bars are 25μm in (A) and 5μm in (A').

(B, C, D) Bright field images of a wild-type juvenile *scospondin-GFP$^{ut24/+}$* (B), *Et(druk-GFP$^{dut26/+}$)* (C), and *Et(druk-GFP$^{dut26/+}$); scospondin-GFP$^{ut24/+}$* (D) displaying the onset of mild scoliosis. Scale bar is 1mm, standard length in upper right corner.

(B', C', D') Inverted greyscale maximal Z-projections of confocal images of the same fish in B, C and D to highlight the spinal cord. At 19 dpf, in wild-type *scospondin-GFP$^{ut24/+}$* we observe high expression of the Reissner fiber (100%, n=14 size range 6.3-6.8mm)(B'), in scoliosis mutant *Et(druk-GFP$^{dut26/+}$)*; +/+ the Reissner fiber is not labeled but some spinal

cord cells express GFP (n=6 size range 6.0-6.5mm), while in double mutant *Et(druk-GFP*$^{dut26/+}$); *scospondin-GFP*$^{ut24/+}$ we observed curvature of the spinal canal and a complete loss of a Reissner fiber (94%, n=16 size range 6.1–7.0mm). Scale bars are 10μm.

(E, F) Inverted greyscale maximal Z-projections of confocal imaging of AFRU-stained zebrafish embryos at 1 dpf (30hpf). The Reissner fiber is observed in heterozygous kinesin family member 6 (*kif6*$^{sko/+}$) and homozygous *kif6*^{sko} mutants (8/8, E-E"). Scale bars are 10μm.

(G-H") Inverted greyscale maximal Z-projections of confocal imaging of AFRU and ZO-1 stained zebrafish at 3 dpf. ZO-1 localizes to tight junctions and shows the location of the central canal epithelium. Heterozygous *kif6*$^{sko/+}$ animals have an intact Reissner fiber in the central canal (13/13) (G-G"), whereas in homozygous *kif6*^{sko} the Reissner fiber is disassembled and Reissner material fills the space of the central canal (12/13) (H-H"). Scale bars are 25μm

(I-J) Merge of maximal Z-projections of confocal imaging of AFRU and ZO-1 stained zebrafish at 5 dpf. Heterozygous *kif6*$^{sko/+}$ animals have an intact Reissner fiber in the central canal (I), but in homozygous *kif6*^{sko} animals diffuse Reissner material fills the central canal lumen (J). Scale bars are 10μm.